

# Structure of Earth's outer radiation belt inferred from long-term electron flux dynamics

D. Vassiliadis,<sup>1</sup> A. J. Klimas,<sup>2</sup> R. S. Weigel,<sup>3</sup> D. N. Baker,<sup>3</sup> E. J. Rigler,<sup>3</sup> S. G. Kanekal,<sup>4</sup> T. Nagai,<sup>5</sup> S. F. Fung,<sup>2</sup> R. W. H. Friedel,<sup>6</sup> and T. E. Cayton<sup>6</sup>

Received 13 March 2003; revised 13 July 2003; accepted 11 September 2003; published 15 October 2003.

[1] We map the spatial structure of the electron belts over their radial range ( $L = 1-11 R_E$ ) using a total of 25 years of observations by NASA, ISAS, and GPS spacecraft. Correlation analysis reveals significant radial structuring of the outer belt and identifies three regions, while earlier single-spacecraft studies are used to interpret the results. The central region  $P_1$  ( $L = 4.1-7.5 R_E$ ) has a well-known slow response (2–3 days) most probably due to shear-hydrodynamic effects of the interplanetary medium, which excite ULF waves at low latitudes. In the innermost region  $P_0$  ( $L = 3.0-4.1 R_E$ ) the electron response is rapid ( $<1$  day). It appears related to solar wind ram-hydrodynamic inputs (compressions) and/or time-varying interplanetary electric and magnetic fields. Region  $P_2$  ( $L > 7.5 R_E$ ) has a much weaker brief response to magnetic field orientation and low interplanetary plasma velocities, anticorrelated with the other two regions. The findings and, in addition, the solar-cycle modulation of the region size strongly suggest that the solar wind excites nonlinear response modes in the inner magnetosphere which are prototypically revealed in the three regions. Given this spatial variability, the optimal approach to next-generation modeling and electron storm forecasting may differ considerably for each region.

**INDEX TERMS:** 2720 Magnetospheric Physics: Energetic particles, trapped; 2730 Magnetospheric Physics: Magnetosphere—inner; 2740 Magnetospheric Physics: Magnetospheric configuration and dynamics; 2784 Magnetospheric Physics: Solar wind/magnetosphere interactions. **Citation:** Vassiliadis, D., A. J. Klimas, R. S. Weigel, D. N. Baker, E. J. Rigler, S. G. Kanekal, T. Nagai, S. F. Fung, R. W. H. Friedel, and T. E. Cayton, Structure of Earth's outer radiation belt inferred from long-term electron flux dynamics, *Geophys. Res. Lett.*, 30(19), 2015, doi:10.1029/2003GL017328, 2003.

## 1. Introduction

[2] The first space missions revealed an energetic-particle (“radiation”) environment stretching beyond Earth's ionosphere [Van Allen and Frank, 1959], whose large-scale structure inherits the azimuthal symmetry of the magnetic

field. The invariant-preserving motion of particles reduces the effective geometry to radial for timescales of  $>1$  day. The primary length scale is the geocentric distance  $L$  of the particle's field line intersection with the equatorial plane. The slot region, a particle sink at  $1 < L < 2 R_E$  due primarily to wave-particle interaction, divides the electron belt into the inner and outer zone. Further out than  $L = 10-12 R_E$  on Earth's nightside, the belts overlap with the magnetospheric plasma sheet.

[3] Radiation belt particle fluxes exhibit a complex spatial and temporal variability. Relativistic electron fluxes span more than two orders of magnitude in intensity during storms that last several days. Figure 1 shows the logarithm of the directional flux of 2–6 MeV electrons,  $j_e(t; L) \equiv \log J_e(t; L)$ , at equally spaced  $L$  shells over the year 1993. Daily-average fluxes are obtained by the Proton-Electron Telescope (PET) on NASA's Solar, Anomalous, and Magnetospheric Particle Explorer (SAMPEX) [Baker et al., 1993]. We use measurements from SAMPEX/PET and three other spacecraft, at overlapping times, orbit altitudes, and energy ranges, to cross-validate results and minimize possible effects of altitude and detector energy range.

## 2. Methodology and Results

[4] We have mapped the radiation-belt structure by quantifying the electron flux variability over the entire radial range of the inner magnetosphere. The two-point radial correlation function between flux histories at  $L_1$  and  $L_2$  is a diagnostic for the extent and degree of coherence in the belts:

$$C(L_1, L_2) = \frac{1}{T \sigma_{j(L_1)} \sigma_{j(L_2)}} \int_0^T \delta J(t; L_1) \delta J(t; L_2) dt \quad (1)$$

The long-term-average flux at each  $L_i$  has been removed,  $\delta J(t; L_i) \equiv J(t; L_i) - \bar{J}(L_i)$ , and  $\sigma_{j(L_i)}$  is the corresponding standard deviation. For SAMPEX/PET,  $T$  is the interval 1993–2000.

[5] Rather than slowly-varying with  $L$  over the outer zone, according to standard models [e.g., Heynderickx, 2002], the correlation function (1) has a three-block structure (Figure 2 at resolution  $\delta L = 0.1 R_E$ ). In each block the fluxes vary in time, but remain highly coherent, while the cross-correlation between blocks remains low. We measure each region's extent using the first diagonal cross-section of  $C(L, L)$ , i.e., finding the minima of  $C(L, L + \delta L)$ . Numerical results are checked versus visual inspection and compared

<sup>1</sup>Universities Space Research Association, NASA/Goddard Space Flight Center, USA.

<sup>2</sup>NASA/Goddard Space Flight Center, USA.

<sup>3</sup>Laboratory for Astrophysics and Space Physics, University of Colorado, USA.

<sup>4</sup>Department of Physics, Catholic University of America, USA.

<sup>5</sup>Tokyo Institute of Technology, Japan.

<sup>6</sup>NIS-2 Division, Los Alamos National Laboratory, USA.

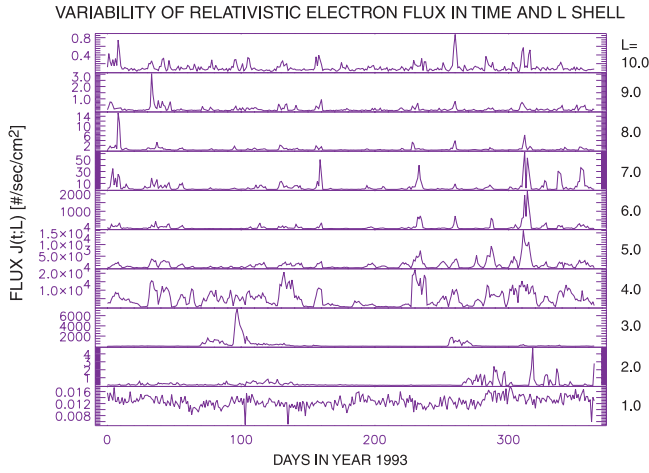


**Figure 1.** Radial and temporal variations of the trapped electron flux span many orders of magnitude: daily-averaged directional fluxes of 2–6 MeV electrons measured by SAMPEX/PET at equidistant L shells in the range  $L = 1.0$ – $10.0$  in 1993.

for successive years (and different spacecraft), identifying the following regions:

### 2.1. Regions $P_0$ and $P_1$

[6] At  $L = 3.0$ – $4.1$  and  $L = 4.1$ – $7.5$ , respectively, they constitute the main body of the outer zone. By its size and

flux content,  $P_1$  in particular contains the vast majority of relativistic electron flux in the belts. To interpret the differences between  $P_0$  and  $P_1$  we compare  $C(L_1, L_2)$  with the response of the flux to the solar wind. In prior work [Vassiliadis *et al.*, 2002] we used simple filter models to approximate the response of the SAMPEX log-flux at shell  $L_i$  to the primary interplanetary driver, the solar wind speed  $V_{sw}$ :

$$j_e(t; L_i) = \int_{-T_s}^T H(\tau; L_i) V_{sw}(t - \tau) d\tau + \varepsilon(t) \quad (2)$$

where  $T_s = 5$  d,  $T = 20$  d, and  $\varepsilon(t)$  is the fit residual. The impulse response  $H(\tau; L)$  has peaks consistent with  $P_0$  and  $P_1$  (Figure 2b) although their exact positions vary with the interplanetary input chosen (also there is no peak corresponding to  $P_2$ ). Time  $\tau = 0$  represents the time of solar wind impact at the magnetopause.  $P_1$  responds slowly to the solar wind variation with the peak response amplitude at  $L = 5.3 \pm 0.9 R_E$  on day  $\tau = 2$ . The four-decade-long historical record from the geosynchronous orbit reflects primarily this response [Paulikas and Blake, 1979]. High-speed structures in the solar wind are geoeffective in  $P_1$  (mainly streams and secondarily shocks and interplanetary products of coronal mass ejections). The peak in  $H(\tau; L)$  is consistent with the longest-correlation L shell from (1), which occurs at  $L = 5.4 \pm 0.7 R_E$ .

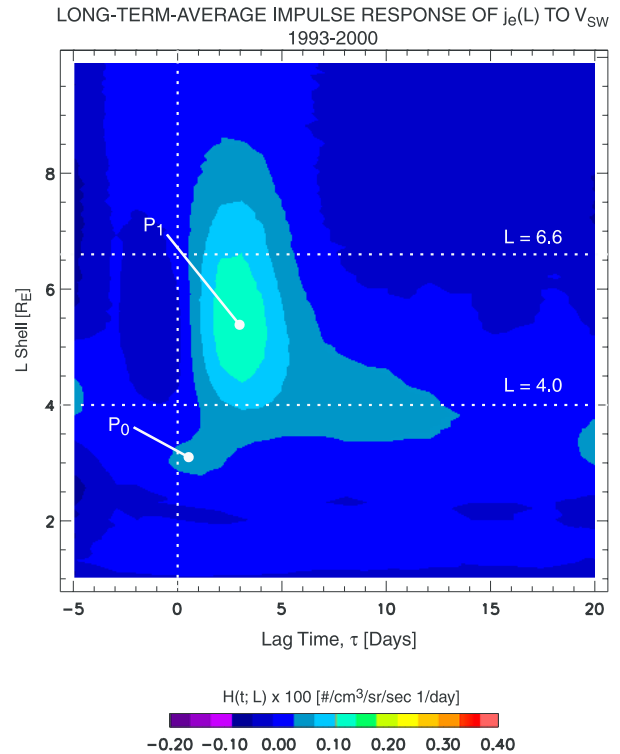
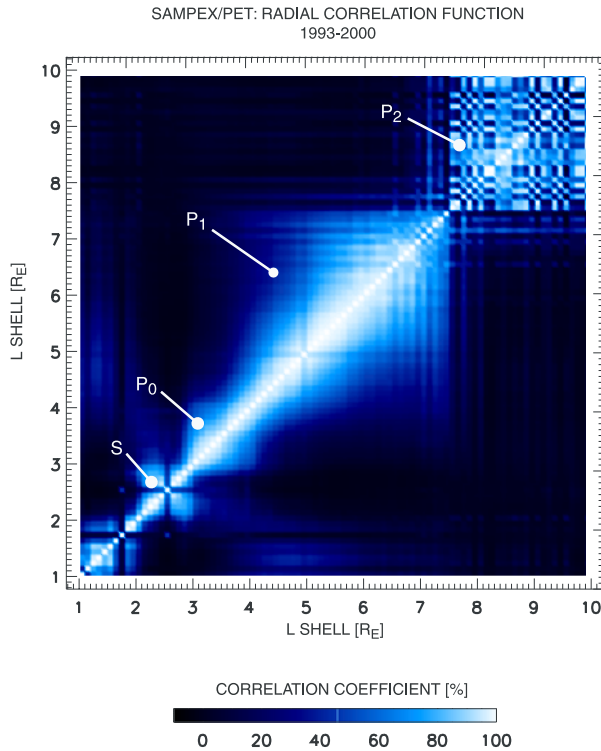


**Figure 2.** (a) Two-point radial correlation function (1) for the 2–6 MeV flux measured by SAMPEX/PET over 1993–2000. Regions  $P_0$ ,  $P_1$ , and  $P_2$ , stand out as distinct blocks with low cross-correlations between them which suggests different flux dynamics and probably locally-dominant acceleration and transport processes. The slot (S) has a characteristic quadrupole pattern. (b) Regions  $P_0$  and  $P_1$  of Figure 2a are clearly seen in the impulse response of the SAMPEX/PET log-flux to the solar wind speed  $V_{sw}$ . Note the difference in response duration. Region  $P_2$  is not detected because its fluxes are of low amplitude and brief duration [after Vassiliadis *et al.*, 2002].

[7] The  $P_0$  response is significantly faster with its peak occurring at  $\tau = 1$  day or less. This is probably the response responsible for observations of rapid, deep ( $L < 4.0$ ) particle injection in recent electron storms (e.g., in May 1997 [Baker *et al.*, 1998] and May 1998; see also [Fung and Tan, 1998]). The storms were induced by high-B-field magnetic clouds in the solar wind and the electron flux responded in tens of minutes to several hours after impact.

[8] Thus the relative geoeffectiveness of solar wind structures (here streams vs. magnetic clouds) varies for each region. This is most probably the result of several mechanisms whose net effect is maximized in a specific L range: for  $P_1$  such processes include ULF wave generation due to viscous-type interactions [Farrugia *et al.*, 2001] and their resonant absorption by low-energy electrons [Hudson *et al.*, 1999; Elkington *et al.*, 2003]. A “seed” low-energy population appears before or simultaneous to the wave growth, as a result of magnetic substorms and other effects of magnetic reconnection. No specific mechanisms have been identified for  $P_0$ , although our ongoing research suggests that the role of the interplanetary density  $\rho_{sw}$  and magnetic field  $B_z$  are much more significant for this region than for  $P_1$ .

## 2.2. The $P_2$ Region

[9] At radial distances  $L > 7.5 R_E$  electron fluxes are much lower than in  $P_0$  or  $P_1$ . The SAMPEX count rates are fairly low at those altitudes so the  $P_2$  block in Figure 2a appears stippled. A clearer view is provided by ISAS spacecraft EXOS-D (Akebono) [e.g., Obara *et al.*, 2000] at an apogee 16 times higher than SAMPEX. Its Radiation Data Monitor provides measurements with few dropouts and therefore correlations which are continuous in L. A  $C(L_1; L_2)$  diagram, very similar to Figure 2a, is calculated from the 2.5-MeV integral omnidirectional flux. Because of RDM's higher count rates the diagram can be obtained from a single year of data (period: 1989–2000) and region  $P_2$  appears as a continuous (not stippled) block. Similar diagrams are also obtained from fluxes at two lower-energy ranges, with a weak scaling of the regional boundaries on energy.

[10] The outer boundary of  $P_2$  is estimated from a third spacecraft, EXOS-C (Ohzora), whose HEP dataset, at energies 0.19–3.2 MeV, overcomes certain L-shell limitations of the SAMPEX and Akebono datasets. Correlation analysis from 3.4 years of  $j_e(t; L)$  shows that  $P_2$  extends as high as  $L = 20 R_E$  (Fluxes at higher L shells are not reliable due to uncertainties of magnetic-field mapping.) Therefore these fluxes are measured well within the inner plasma sheet.

[11] The sharp transition between  $P_1$ – $P_2$  at  $L = 7.5 R_E$  is remarkable given the smooth variation of  $j_e(t; L)$  with L. This effect is due to the magnetopause limiting the region of long-term trapping. The magnetopause dayside position is normally at 9–10  $R_E$ , but interplanetary pressure increases temporarily push the boundary even within the geosynchronous orbit. Fluxes at  $L > 7.5 R_E$  are therefore marginally trapped in the long-run: using a lagged correlation function instead of the correlation coefficient (1) shows that the effective average lifetime of trapped flux is only 2 days in  $P_2$  as opposed to  $>10$  days for  $P_1$ . As a result, the trapping capacity of  $P_2$  is much lower than that of  $P_0$  and  $P_1$ .

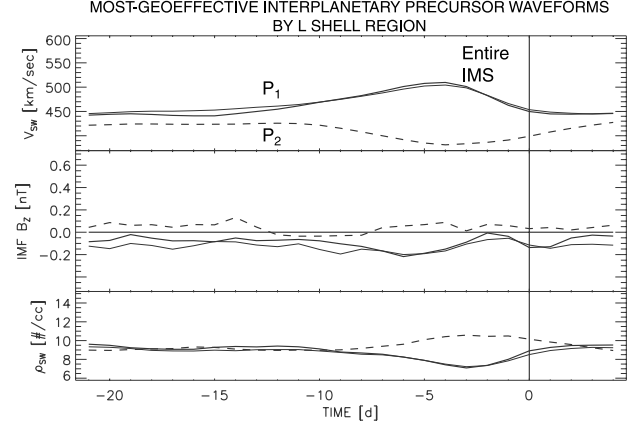


**Figure 3.** Precursor analysis highlights the differences on each side of the  $P_1$ – $P_2$  boundary: A geoeffective interplanetary structure (the “precursor”) produces a subsequent disturbance in the flux levels over a range of L shells. Each panel shows an averaged precursor variable: solar wind velocity (cf. equation (3); relevant for viscous-type interactions), IMF  $B_z$  component (relevant for magnetic reconnection), and solar wind density. Each curve is the average of 731 events, which comprise the upper quartile of SAMPEX/PET L-integrated fluxes over 8 years. (i) solid, heavy: precursors for the entire inner magnetosphere,  $L = 1.1$ – $10.0$ . (ii) Solid, regular:  $L = 4.1$ – $7.0$ , representative of region  $P_1$ . (iii) Dashed:  $L = 8.1$ – $9.0$ , representative of  $P_2$ .

[12] To better distinguish between  $P_1$  and  $P_2$  we revisit our earlier work on precursor analysis [Vassiliadis *et al.*, 2003]. There we determined the geoeffective profiles of solar wind and IMF variables preceding a high-value, spatially integrated log-flux. While the analysis was based on a single spacecraft (SAMPEX) and energy range, it provides guidance here. For the activity over a range  $[L_1, L_2]$  at time  $t$  a precursor was defined from  $T$  recent  $V_{sw}$  measurements:

$$\mathbf{I}(t) \equiv [V_{sw}(t-T), V_{sw}(t-T+1), \dots, V_{sw}(t-1), V_{sw}(t)]. \quad (3)$$

Similar profiles were defined from the IMF  $B_z(t)$  component and the solar wind density  $\rho_{sw}(t)$  and other variables. Precursors to the most active days at a given L shell change abruptly across  $L = 7.0 \pm 1.0$ : Representative profiles in Figure 3 show that  $P_1$ 's precursor is of low density and high speed, and lasts 5–7 days, i.e., a high-speed stream of well-known geoeffectiveness [Paulikas and Blake, 1979]. In contrast, the precursor geoeffective in  $P_2$  is a high-density, low-speed structure. Also the IMF  $B_z$  precursor for  $P_1$  is negative, consistent with dayside magnetic reconnection and seed-electron production, while for  $P_2$  it is positive, implying a weak nightside reconnection poleward of the cusp. The same contrast is seen in IMF  $|B|$  and  $D_{st}$ -index profiles. This clearly suggests that fluxes in  $P_2$  intensify during very different interplanetary conditions than in  $P_1$  and therefore the respective coupling mechanisms must be very different. Region  $P_2$  appears to be associated with an inflated magnetosphere relative to the solar wind conditions giving rise to  $P_0$  and  $P_1$ . (Note

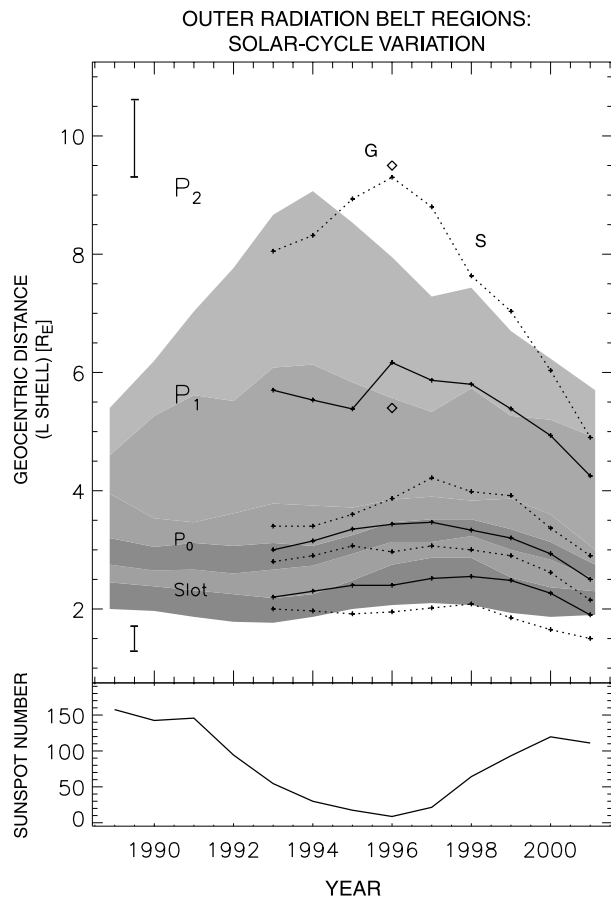


**Figure 4.** Upper panel: solar-cycle variation of the radial extent of the  $P_1$  regions as determined from  $C(L, L)$ . Akebono/RDM measurements in 1989–2001 are shown as shaded regions. A change in color represents a boundary while a change in shading within a region identifies the  $L$  shell with the widest correlation length. Lines (S) denote region centers (solid) and boundaries (dotted) from SAMPEX/PET fluxes. Diamonds (G) denote measurements by GPS NS-33 in 1996 for the center and outer boundary of  $P_1$ . Vertical bars indicate the average uncertainty in the measurements, which increases with  $L$ . Lower panel: annual sunspot number.

that precursors for  $P_0$  do not differ markedly from those of  $P_1$  for these daily-average data.)

### 2.3. Other Regions

[13] Other regions identified in the correlation function diagram include the slot region at  $2.0 < L < 3.0 R_E$  which produces a characteristic quadrupole pattern (Figure 2a): its center, at  $\sim 2.6 R_E$ , is poorly correlated with other parts of the belts, while its two edges are strongly correlated with each other. The high correlation suggests that the fluxes vary in a synchronized manner over long periods of time, i.e., precipitation occurs at similar rates at the slot edges and may involve long-range wave fields. Also distinguishable in the  $C(L_1, L_2)$  graph is the inner zone at  $L < 2.0$ .

### 3. Solar Cycle Variability

[14] At long time scales, the region size is modulated by the interplanetary input (Figure 4). The radial extent of  $P_1$

decreases from solar minimum [1995] to maximum [2001]: Shocks and coronal mass ejections (CMEs), which increase in occurrence during the ascending part of the cycle [e.g., Richardson *et al.*, 2001], continually compress and energize the magnetosphere. While they lead to electron storms, they also erode the outer part of  $P_1$  which is replaced by the “quasitrapped”  $P_2$  fluxes. A solar cycle variation is also evident for  $P_0$ . SAMPEX and Akebono measurements are fairly consistent through the cycle and agree with a fourth spacecraft, GPS NS-33, which is limited to  $L > 4.0$  (only data from 1996 have been examined for NS-33). The modulation of the individual regions is in agreement with earlier results on the periodicity of the total trapped electron flux and its response [Baker *et al.*, 1999; Li *et al.*, 2001; Vassiliadis *et al.*, 2002].

### 4. Discussion

[15] The complex temporal patterns of the relativistic electron flux reveal a structured inner magnetosphere, not expected from earlier, more spatially-limited, observations, but in agreement with findings of magnetospheric coherence [e.g., Kanekal *et al.*, 2001]. Correlation analysis shows that the planetary field configuration allows for three distinct trapping regions with markedly different physical sizes and trapping capacities. The regions retain their identity through the solar cycle and in response to interplanetary parameters. The correlation structure contrasts the effects of the slow “shear-hydrodynamic” coupling on fluxes in  $P_1$ , through viscous interaction, wave excitation, and diffusion, with a rapid “ram-hydrodynamic” coupling for  $P_0$ , probably related to  $B_z$  and  $\rho_{SW}$ , or the Northward- $B_z$  coupling for  $P_2$  with a possibly significant role for cusp acceleration [Sheldon *et al.*, 1998]. The large-scale dynamics of each region arise as a prototypical nonlinear mode of a planetary magnetosphere excited by the time-variable solar wind.

[16] **Acknowledgments.** We thank M.-C. Fok and T. E. Moore for discussions on magnetospheric dynamics, and A. Szabo and V. Osherovich for discussions on transient solar wind structures. NASA/NSSDC provided solar wind and IMF data.

### References

- Baker, D. N., G. M. Mason, O. Figueroa, G. Colon, J. G. Watzin, and R. M. Aleman, An overview of the Solar, Anomalous, and Magnetospheric Particle Explorer (SAMPEX) mission, *IEEE Trans., Geosci. Rem. Sens.*, 31(3), 531–541, 1993.
- Baker, D. N., T. I. Pulkkinen, X. Li, S. G. Kanekal, K. W. Ogilvie, R. P. Lepping, J. B. Blake, L. B. Callis, G. Rostoker, H. J. Singer, and G. D. Reeves, A strong CME-related magnetic cloud interaction with the Earth's magnetosphere: ISTP observations of rapid relativistic electron acceleration on May 15, 1997, *Geophys. Res. Lett.*, 25(15), 2975–2978, 1998.
- Baker, D. N., S. G. Kanekal, T. I. Pulkkinen, and J. B. Blake, Equinoctial and solstitial averages of magnetospheric relativistic electrons: A strong semiannual modulation, *Geophys. Res. Lett.*, 26(20), 3193–3196, 1999.
- Elkington, S. R., M. K. Hudson, and A. A. Chan, Resonant acceleration and diffusion of outer zone electron in an asymmetric geomagnetic field, *J. Geophys. Res.*, 108(A3), 1116, 2003.
- Farrugia, C. J., F. T. Gratton, and R. B. Torbert, Viscous-type processes in the solar wind-magnetosphere interaction, *Space Sci. Rev.*, 95, 1–2, 443–456, 2001.
- Fung, S. F., and L. C. Tan, Time correlation of low-altitude relativistic trapped electron fluxes with solar wind speeds, *Geophys. Res. Lett.*, 25(13), 2361–2364, 1998.
- Heynderickx, D., Radiation belt modelling in the framework of space weather effects and forecasting, *J. Atm. Sol. -Terr. Phys.*, 64(16), 1687–1700, 2002.



- Hudson, M. K., S. R. Elkington, J. G. Lyon, C. C. Goodrich, and T. J. Rosenberg, Simulation of radiation belt dynamics driven by solar wind variations, *Sun-Earth Plasma Connections*, J. L. Burch, R. L. Carovillano, and S. K. Antiochos (Eds.), Geophysical Monograph 109, AGU, Washington, D.C., 1999.
- Kanekal, S. D., D. N. Baker, and J. B. Blake, Multisatellite measurements of relativistic electrons: Global coherence, *J. Geophys. Res.*, 106(A12), 29,721–29,732, 2001.
- Li, X., et al., Long term measurements of radiation belts by SAMPEX and their variations, *Geophys. Res. Lett.*, 28(20), 3827–3830, 2001.
- Obara, T., et al., Energetic electron variation in the outer radiation zone during early May 1998 magnetic storm, *J. Atm. Sol. -Terr. Phys.*, 62(15), 1405–1412, 2000.
- Paulikas, G. A., and J. B. Blake, Effects of the solar wind on magnetospheric dynamics: Energetic electrons at the synchronous orbit, in: *Quantitative Modeling of Magnetospheric Processes*, W. P. Olson (Ed.), Geophysical Monograph 21, AGU, Washington, D.C., 1979.
- Richardson, I. G., E. W. Cliver, and H. V. Cane, Sources of geomagnetic storms for solar minimum and maximum conditions during 1972–2000, *Geophys. Res. Lett.*, 28(13), 2569–2572, 2001.
- Sheldon, R. B., H. E. Spence, J. D. Sullivan, T. A. Fritz, and J. Chen, The discovery of trapped energetic electrons in the outer cusp, *Geophys. Res. Lett.*, 25, 1825–1828, 1998.
- Van Allen, J. A., and L. A. Frank, Radiation around the Earth to a radial distance of 107,400, *Nature*, 183(4659), 430–434, 1959.
- Vassiliadis, D., A. J. Klimas, S. G. Kanekal, D. N. Baker, and R. S. Weigel, Long-term average, solar-cycle, and seasonal response of magnetospheric energetic electrons to the solar wind speed, *J. Geophys. Res.*, 10.1029/2001JA000506, 2002.
- Vassiliadis, D., R. S. Weigel, A. J. Klimas, S. G. Kanekal, and R. A. Mewaldt, Modes of energy transfer between the solar wind and the inner magnetosphere, *Phys. Plasmas*, 10(2), 463–473, 2003.
- 
- D. Vassiliadis, Universities Space Research Association, NASA/Goddard Space Flight Center, USA. (vassi@lepgst.gsfc.nasa.gov)
- A. J. Klimas and S. F. Fung, NASA/Goddard Space Flight Center, USA.
- R. S. Weigel, D. N. Baker, and E. J. Rigler, Laboratory for Astrophysics and Space Physics, University of Colorado, USA.
- S. G. Kanekal, Department of Physics, Catholic University of America, USA.
- T. Nagai, Tokyo Institute of Technology, Japan.
- R. W. H. Friedel and T. E. Cayton, NIS-2 Division, Los Alamos National Laboratory, USA.